

# Direct observation of Pancharatnam geometric phase in a quenched topological system

Tian Tian<sup>1,3</sup>, Yongguan Ke<sup>2</sup>, Liang Zhang<sup>1,3</sup>, Shaochun Lin<sup>1,3</sup>, Zhifu Shi<sup>1,3,5</sup>, Pu Huang<sup>4</sup>, Chaohong Lee<sup>2,6,\*</sup>, and Jiangfeng Du<sup>1,3,5,\*</sup>

<sup>1</sup>*CAS Key Laboratory of Microscale Magnetic Resonance and Department of Modern Physics, University of Science and Technology of China, Hefei 230026, China*

<sup>2</sup>*Laboratory of Quantum Engineering and Quantum Metrology, School of Physics and Astronomy, Sun Yat-Sen University (Zhuhai Campus), Zhuhai 519082, China*

<sup>3</sup>*Synergetic Innovation Center of Quantum Information and Quantum Physics, University of Science and Technology of China, Hefei 230026, China*

<sup>4</sup>*National Laboratory of Solid State Microstructures and Department of Physics, Nanjing University, Nanjing, 210093, China*

<sup>5</sup>*Hefei National Laboratory for Physical Sciences at the Microscale, University of Science and Technology of China, Hefei 230026, China*

<sup>6</sup>*State Key Laboratory of Optoelectronic Materials and Technologies, Sun Yat-Sen University (Guangzhou Campus), Guangzhou 510275, China*

(Dated: June 13, 2022)

Berry phase, the geometric phase accumulated in cyclic adiabatic evolution, has been commonly used to define topological invariants for equilibrium states [1, 2]. Pancharatnam geometric phase, a purely geometric phase accumulated in generic time-evolution, extends the Berry phase to non-adiabatic and non-cyclic dynamics [3, 4]. Theoretically, the Pancharatnam geometric phase can perfectly identify dynamical phase transitions in quenched systems [5, 6], which are analog to equilibrium phase transitions in the Ginzburg-Landau paradigm. However, due to the great challenge in eliminating the dynamical phase during a non-cyclic evolution, it is hard to observe the Pancharatnam geometric phase in dynamical phase transitions. Here, we directly observe the Pancharatnam geometric phase after sudden quenches from a topological edge state in the Su-Schrieffer-Heeger model, which is realized by a reconfigurable array of nanomechanical oscillators. Due to the chiral symmetry in our system, the initial edge state equally populates all symmetrical pairs of final eigenstates and so that the dynamical phase is naturally eliminated. We found that, the Pancharatnam geometric phase jumps  $\pi$  at each critical time when dynamical phase transition takes place, otherwise the Pancharatnam geometric phase keeps unchanged. This work not only provides a quantitative method to identify dynamical phase transitions, but also paves the way to reveal the bulk-edge correspondence for dynamical phase transitions in topological systems [7].

Topological phases have attracted tremendous attentions and interests for their significant values of fundamental physics as well as potential applications [8–12]. Berry phase provides a basic ingredient to understand the topological phases in the adiabatic and cyclic dynamics [2]. Many topological effects such as quantum Hall effects, characterized by topological invariants, originate from the Berry phase after adiabatically sweeping

eigenstates over the parameter space. However, Berry phase cannot capture the topological effects in the non-adiabatic and non-cyclic dynamics, namely, the dynamical vortices or emerging ring structure in the quenched dynamics [13, 14].

Pancharatnam geometric phase (PGP) plays an important role to identify the non-equilibrium effects in a quenched system [6, 15–18]. In analog to phase transition in equilibrium system, dynamical phase transition (DPT) is an outstanding non-equilibrium effect which is denoted by the non-analytic behaviors of rate function (i.e. the logarithm function of returning probability to initial state) driven by time [5, 18]. A theory indicates that the PGP jumps  $\pi$  at each DPT point, giving exact quantitative hallmark of DPT [6]. Furthermore, dynamical winding number based on PGP can be also served as a dynamical topological invariants to explain the dynamical vortices [17]. Measuring PGP will be the first step to understand the relation between topological phase and non-equilibrium dynamics. Although dynamical phase transitions (DPTs) have been observed in trapped-ion and cold-atom systems [13, 19], it's a great challenge to directly measure PGP [20, 21] and demonstrate its relation to DPT, because PGP always accompanies with dynamical phase.

In this letter, we give the experimental observation of PGP and its jump as hallmarks of DPT in the Su-Schrieffer-Heeger (SSH) model [22], which is realized by eight nanomechanical oscillators. The coupled oscillators play the role of an artificial lattice [23], which can be easily fabricated by the traditional MEMS/NEMS processing and flexibly engineered by capacitive coupling [24]. Sudden quenches between different structures are easily configured by tuning the different coupling voltages between oscillators. The initial state preparation and high-resolution measurement are enable with the standard magneto-motive technique [25]. Since the dynamical phase is naturally eliminated, we directly observe the PGP jumps  $\pi$  at critical time by demodulating the motion of the edge oscillator. We also observe the non-analytic behaviors of the rate function, which indicate

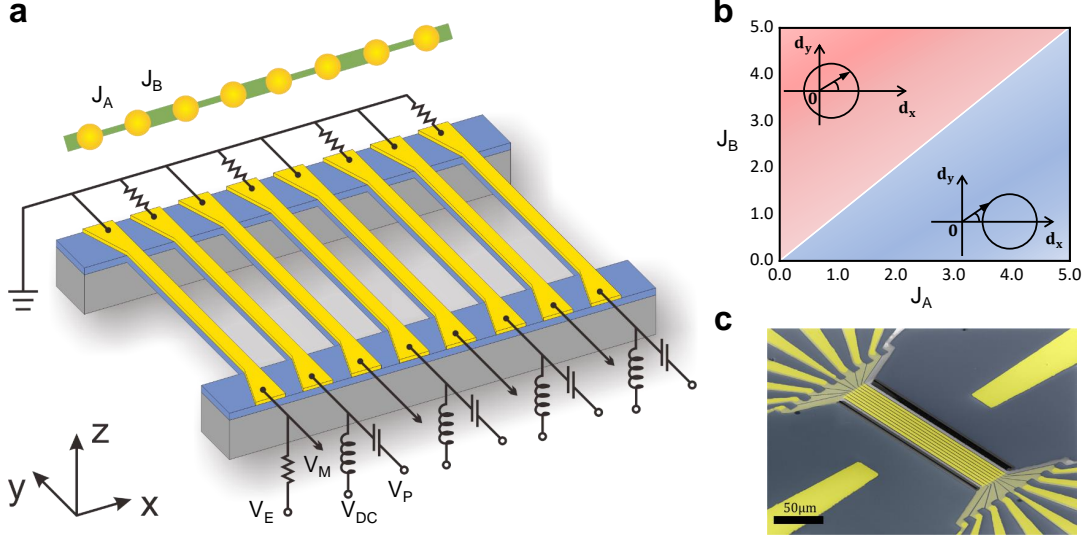


Figure 1. **Nanomechanical oscillators for simulating SSH model.** **a**, The sample of eight almost identical nanomechanical oscillators (doubly clamped beams) is fabricated by 100nm thick silicon nitride (dark blue) coat with a thin layer of gold. For every oscillator, the first mode of vibration (along  $z$  axis) is used in this work. The nearest-neighbor parametric couplings are realized by applying sum of  $V_{DC}$  and  $V_{AC}$  between every two adjacent oscillators. The unit cell of SSH chain is represented by two adjacent oscillators. The hopping strength (green lines) of SSH can be tuned by parametric couplings. Magnetic field is applied along  $x$  axis for excitation ( $V_E$ ) and detection (black arrows). **b**, Equilibrium phase diagram of SSH model. If intracell hopping  $J_A$  is larger than intercell hopping  $J_B$ , SSH chain is trivial and the winding number  $\mathcal{W} = 0$ . Otherwise, the SSH chain is topological and the winding number  $\mathcal{W} = 1$ . **c**, False-color scanning electron micrograph of the sample.

the DPTs. This is the first time that PGP and DPTs are observed simultaneously under open boundary condition.

We study the quench dynamics in a 1D topological model—SSH chain [22]. This model describes an 1D lattice with two sites per unit cell, and its hopping distribution are staggered. The Hamiltonian with chiral symmetry is

$$\hat{H} = (-J_A \sum_{j=\text{odd}} |j\rangle\langle j+1| - J_B \sum_{j=\text{even}} |j\rangle\langle j+1|) + h.c. \quad (1)$$

where  $|j\rangle$  is the state of exciting the  $j$ -th site,  $J_A$  and  $J_B$  are intracell and intercell hopping respectively showed in the top of Fig. 1a. The topological invariant of SSH model is characterized by winding number [26]. In momentum space, the Hamiltonian is given as  $\hat{H}(k) = \mathbf{d}(k) \cdot \boldsymbol{\sigma}$  with the Pauli matrices  $\boldsymbol{\sigma}$ . The trajectory of  $\mathbf{d}(k)$  does not encircle the origin point when  $J_A > J_B$ , so the winding number is  $\mathcal{W} = 0$  and the structure is topological trivial. On the conversely, the winding number is  $\mathcal{W} = 1$  and the structure is topological nontrivial when  $J_A < J_B$ , see Fig. 1b. According to bulk-edge corresponding, there exist topological edge state under open boundary condition if the bulk invariant is nontrivial. Under this condition, the energy spectrum of two SSH topological phase are different, which are showed in Fig. 2a (trivial phase) and Fig. 2c (nontrivial phase). There exist topological edge states/zero modes in the band gap of topological nontrivial phase. Thus, we can distinguish topological trivial and nontrivial structures

by the winding number or the existing of edge states. In Fig. 1b, we show the equilibrium topological phase diagram in the  $(J_A, J_B)$  plane.

We configure the 1D tight-binding model by a reconfigurable array in experiment, see Fig. 1a. The array consists of eight almost identical oscillators (doubly clamped beams). Every unit cell of SSH model includes two adjacent oscillators. The intracell and intercell hopping are controlled by different nearest-neighbor parametric couplings, which are realized by applying voltage  $V_{DC} + V_{AC}$  between two oscillators. The classical motion equations of coupled oscillators can be fully mapped to the Hamiltonian of SSH model (see Methods). We choose 20Hz and 60Hz coupling strength alternately to realize a topological phase in SSH model. On the contrary, we realize a trivial phase by choosing 60Hz and 20Hz alternately. These two structures are determined by measuring the stabilized frequency response of the first oscillator (see Supplementary Information).

We study the quench dynamics of a edge state from  $\hat{H}_i : J_A/J_B \rightarrow 0$  to (i)  $\hat{H}_{f1} : J_A > J_B$  and (ii)  $\hat{H}_{f2} : J_A < J_B$ . The initial state is prepared at the edge site,  $|\psi(0)\rangle = (1, 0, \dots, 0)^T$ , which is the eigenstate of a large dimeric topological Hamiltonian  $\hat{H}_i$ . The first quench cross the underlying topological phase transition, while the second quench stays in the same topological phase. The evolution of system follows  $|\psi(t)\rangle = e^{-i\hat{H}_f t} |\psi(0)\rangle$  in

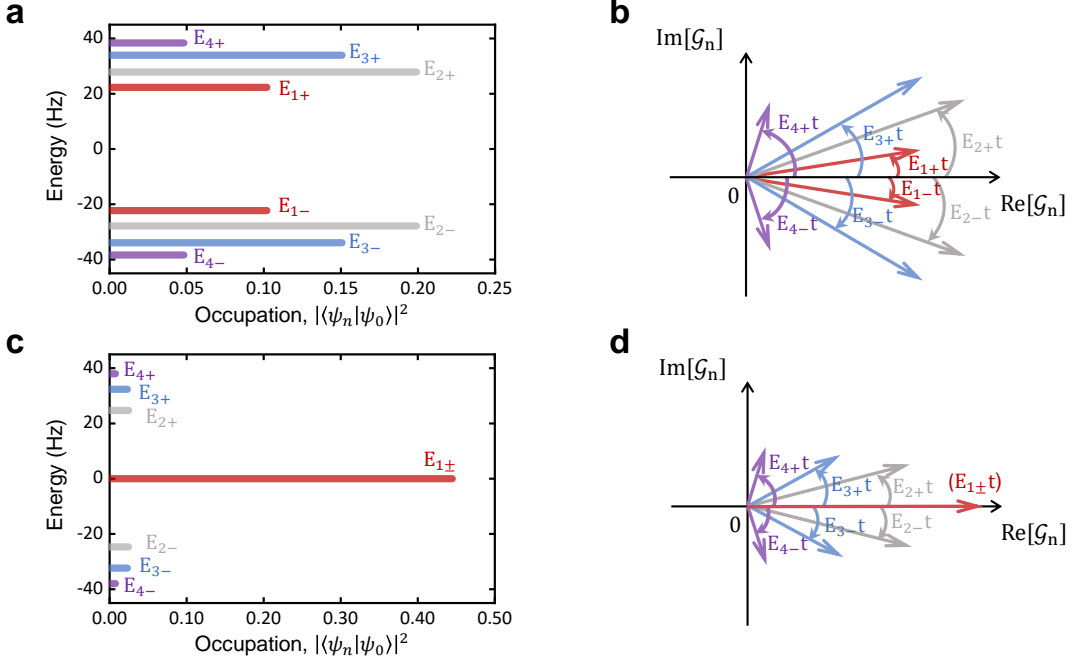


Figure 2. **Symmetric energy spectrum and partial Loschmidt amplitudes.** **a**, The energy band of final trivial SSH Hamiltonian and occupations of the initial edge state in final eigenstates. **b**, The partial Loschmidt amplitude after sudden quench of edge state evolving under a trivial SSH Hamiltonian. **c**, The energy band of final topological SSH Hamiltonian and occupations of the initial edge state in final eigenstates. **d**, The partial Loschmidt amplitude after sudden quench of edge state evolving under a nontrivial SSH Hamiltonian.

quenching paths. The Loschmidt amplitude is given as

$$\mathcal{G}(t) = \langle\psi(0)|\psi(t)\rangle = r(t)e^{i\phi(t)} = \sum_n \mathcal{G}_n(t) \quad (2)$$

where  $r(t)$  is the modulus of Loschmidt amplitude,  $\phi(t)$  is the phase containing a dynamical phase  $\phi^{dyn}(t) = -\int_0^t \langle\psi(s)|\hat{H}_f|\psi(s)\rangle ds$  and PGP  $\phi^P$  [6], and  $\mathcal{G}_n(t) = |\langle\psi_n|\psi(0)\rangle|^2 e^{-iE_n t}$  is partial Loschmidt amplitude with eigenstates  $|\psi_n\rangle$  and eigenvalues  $E_n$  of final Hamiltonian  $\hat{H}_f$ .

Due to the chiral symmetry, the initial edge state equally populates all symmetrical pairs of final eigenstates so that the occupation  $|\langle\psi_{m,-}|\psi(0)\rangle|^2 = |\langle\psi_{m,+}|\psi(0)\rangle|^2$ ,  $m = 1, 2, 3, 4$  for the SSH chain. The occupations are shown in Fig. 2a and c. And the Fig. 2b and d show that, there is always symmetrical part for  $\mathcal{G}_n$  at each moment because of  $E_{m,-} = -E_{m,+}$ . Thus, Loschmidt amplitude  $\mathcal{G}(t) \in \mathbf{R}$  and the phase  $\phi(t)$  of Loschmidt amplitude is 0 or  $\pi$  all the time.

By the same reason, the dynamical phase keeps zero

$$\phi^{dyn}(t) = -\sum_n |\langle\psi_n|\psi(0)\rangle|^2 E_n t = 0 \quad (3)$$

so that  $\phi^{dyn}$  is naturally eliminated and the phase  $\phi(t)$  we measure is directly give the PGP (see Supplementary Information). According to the original definition of DPTs [5, 18], the rate function derived from Loschmidt

amplitude as

$$\lambda(t) = -\frac{1}{N} \ln |\mathcal{G}(t)|^2 = -\frac{1}{N} \ln |r(t)|^2 \quad (4)$$

will become nonanalytic at the critical time when DPTs take place. Thus, when Loschmidt amplitude  $\mathcal{G}(t)$  goes through zeros in quenched dynamics, the DPTs take place while the PGP jumps  $\pi$  [6].

In experiment, quenches of topological edge state in different topological phases are realized by the different pulse sequences (see Supplementary Information). The preparation initial edge state is applying a sinusoidal wave generated by AWG with  $\omega_E$  to the first oscillator. At time  $t = 0$ , we turn on all the coupling voltages between every two adjacent oscillators to realize SSH Hamiltonian  $\hat{H}_f$ . As the time evolves, we measure the vibration of each oscillator with the lock-in amplifier. The measured signal is amplified and demodulated by a reference (generated by AWG). Both the vibrational amplitude and the phase can be extracted from lock-in phase-sensitive detection (see Methods).

The Loschmidt amplitude and the PGP are obtained by the normalized amplitude and the vibration phase of the edge oscillator, respectively. In the quench (showed in Fig. 3a by red arrow) where the topological edge state evolves under the trivial Hamiltonian  $\hat{H}_{f1}$  that coupling strengths are 60Hz and 20Hz alternately, we observe the PGP jumps twice in 40ms evolution from Fig. 3b. In the

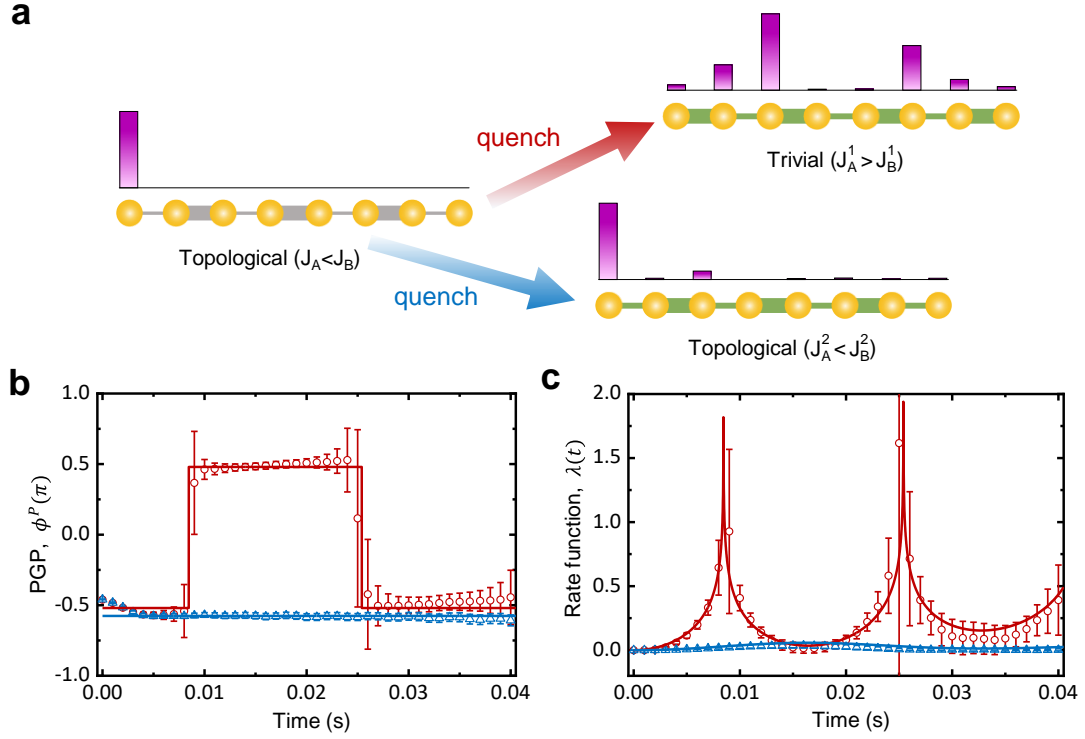


Figure 3. **Dynamical evolution after quench.** **a**, Schematic for the two kinds of sudden quenches in a SSH model with an initial edge state: (i) from topological nontrivial ( $J_A < J_B$ ) to trivial ( $J_A^1 > J_B^1$ ) (red arrow), and (ii) from topological nontrivial ( $J_A < J_B$ ) to nontrivial ( $J_A^2 < J_B^2$ ) (blue arrow). In the quench-(i), the initial edge state will propagate over the entire chain. In the quench-(ii), the initial edge state will dominate the time-evolution. **b**, The PGP in two different quenches in **a**, which is observed from the demodulating phase of the edge oscillator. The PGP jumps  $\pi$  at each critical time in the red quench. The PGP remains unchanged in the blue quench. The initial values of PGP are non-zeros constants because of measuring circuit. **c**, The rate function for two different quenches in **a**, which is derived from the normalized amplitude of the edge oscillator, the non-analytic behavior are obvious at DPTs. All solid lines in **b** and **c** are theoretical results derived from quantum mechanics. All error bars denote statistical confidence of one standard deviations.

quench (showed in Fig. 3a by blue arrow) where the topological edge state evolves under the topological Hamiltonian  $\hat{H}_{f2}$  that coupling strengths are 20Hz and 60Hz alternately, we observe the PGP keeps unchanged in 40ms evolution from Fig. 3b. The initial nonzero PGP result from the external electric circuits, and it does not affect the jump behavior. The experimental results (circles and triangles) in Fig. 3b are measured by averaging 500 times, and they are in great agreement with the theoretical results.

To diagnose the DPTs, we also measure the rate function in these two quenches. We assume that all oscillators have the same decay rates in the short time of evolution, due to the strong coupling strengths much larger than the decay rates, the high quality factors and the small differences between the oscillators. Therefore, all amplitudes can be normalized every moment. We obtain the rate function from the normalized amplitude of the first oscillator in two quenches. and observe non-analytic behaviors of the rate function when the system is quenched across an underlying topological phase transition, see the red circles with error bar in the Fig. 3c. The non-analytic behaviors directly verify the DPTs. For the quench in the

same topological phase, the rate function is always analytic, which suggests that there is no appearance of DPTs, see the blue triangle with error bar. All the experimental results are in good agreement with the theoretical results (represented by solid lines) obtained by solving the quantum mechanical dynamics.

The two different kinds of quenches can be explained by the partial Loschmidt amplitudes in Fig. 2b and d. Each pair of partial Loschmidt amplitudes with  $E_{m,+}$  and  $E_{m,-}$  can be viewed as two vectors rotating around the origin with same length ( $|\langle \psi_{m,\pm} | \psi(0) \rangle|^2$ ) and frequency ( $|E_{m,\pm}|$ ) but opposite direction. Thus, the summation of all these vector pairs gives a total vector along the real axis, representing the real Loschmidt amplitude. The PGP jumps  $\pi$  and DPT takes place as the Loschmidt amplitude changes between positive and negative. In the sudden quench from topological nontrivial to trivial phases, all pairs of vectors rotate around the origin with non-zero frequencies and so that the total vector can always change direction. In the sudden quench from topological nontrivial to nontrivial phases, the Loschmidt amplitude is dominated by the non-rotating vector pair with zero energy ( $|E_{1,\pm}| = 0$ ) and therefore the total



vector will not change its direction.

In summary, by using a reconfigurable nanomechanical array, we directly observe PGP and rate function after quenching the topological edge state in the SSH model. In the quench from underlying topological nontrivial to trivial phase, we observe the  $\pi$  phase jumps in PGP in company with nonanalytic of rate function, indicating the dynamical phase transition. In the quench from underlying topological nontrivial to nontrivial phase, we observe that PGP keeps the same while the rate function is analytic. We build the close relation between the PGP and the rate function for diagnosing the dynamical phase transition. In addition, our system can be used to study more complicated phenomena including interplay between topology, dissipation and nonequilibrium dynamics [27].

## METHODS

**The chain coupled oscillators.** In our study, eight coupled oscillators are realized by nearest-neighboring parametric couplings. The vibrational amplitudes of the oscillators follow the equations of motion,

$$m_j \ddot{x}_j = -m_j \omega_j^2 x_j - L_j(t)(x_{j+1} - x_j) - L_{j-1}(t)(x_{j-1} - x_j) \quad (5)$$

where  $L_j(t) = 2\eta_j \cos[(\omega_{j+1} - \omega_j)t]$  is the time-dependent coupling between the  $j$ -th and  $(j+1)$ -th beams.  $\eta_j$  is the coupling strength which can be controlled by the sum of the applied  $V_{DC}$  and  $V_{AC}$  between the  $j$ -th and  $(j+1)$ -th beams. Using slowly varying complex amplitudes  $\psi_j$  as  $x_j = \sqrt{\hbar\omega_j/(2k_j)}\Re(\psi_j e^{i\omega_j t})$  and rotating wave approximation (see Supplementary Information), the equations of motion can be rewritten as

$$i \frac{\partial}{\partial t} |\psi\rangle = \hat{H} |\psi\rangle \quad (6)$$

where  $\psi_j = \langle j | \psi \rangle$  is made to be normalized as  $\sum_j |\psi_j|^2 = 1$ .  $H$  can be made as SSH model by setting  $\eta_j \sqrt{\omega_j \omega_{j+1}/k_j k_{j+1}}/2 = J_A(J_B)$  when  $i \in \text{odd}(\text{even})$ .

Apart from equation (6), the coherent energy always dissipates into the environment in the actual physics systems. If the decay rate  $\gamma_j$  of each beam is far less than the coupling strength, we can still observe coherent dynamics long before the system decays into the environment. On the other hand, if the beams almost have the same decay rate  $\gamma_j = \gamma$  ( $j = 1, 2, \dots, 8$ ), we can separate the complex amplitude as exponential decay term multiple the coherent term,  $|\psi\rangle = e^{-\gamma t} |\varphi\rangle$ . The dynamics of coherent term  $|\varphi\rangle$  is still governed by the SSH model. Based on the two considerations, we try to decrease the decay rates and make an approximation that the decay rates are almost the same in short evolution time.

**Fabrication of the sample.** The sample is fabricated as doubly clamped beams with  $200\mu\text{m}$  long on wafers composed of a silicon substrate with  $100\text{nm}$  layer of high-stress (1GPa) silicon nitride using the method

of low pressure chemical vapor deposition. Electrodes and the wide beam ( $3\mu\text{m}$ ) are defined by standard ultra-violet lithography. All beams and electrodes are thickened by  $10\text{nm}$  Au. The distance between each two adjacent beams is narrowed to  $500\text{nm}$  by means of e-beam lithography and ion beam etching (remove metal layer). Reactive ion etching is then employed to eliminate silicon nitride layer. Finally, the mechanical beams are suspended by KOH wet etch. These beams are numbered from 1 to 8. The parameters of the first out-of-plane vibrational mode of every beam in experiments are showed in Table S1.

**Measurement Scheme.** The sample is placed in a vacuum of  $3 \times 10^{-6}\text{Pa}$  and cooled to  $77\text{K}$  for the stable frequency and high quality factor. The other measurement circuit at room temperature and all measurements followed the standard magneto-drive method [25]. The standard lock-in amplifiers (The Zurich Instruments HF2LI) are used to measure the frequency-domain spectrums and time-domain measurements. All the frequency generation setups are referencing an external atomic clock to ensure the frequency stability.

It should be pointed that all of oscillators work in linear regime. This can be controlled by the excited strength at the first beam. For any oscillator in linear regime, the relation between amplitude  $|x(\omega)|$  of the vibration and measured voltage amplitude  $|V(\omega)|$  is

$$|x(\omega)| = |V(\omega)|/\xi B L \omega \quad (7)$$

with  $\xi \approx 0.83$  the shape factor of the first vibrational mode.

For the parametric coupling (details in the next section), the time-domain measurement is divided into two parts, the diagrams showed in Fig. S2 and Fig. S3. We measure amplitudes of odd oscillators when applied coupling voltage  $V_P$  and  $V_{DC}$  to even oscillators and measure amplitudes of even oscillators when applied coupling voltage  $V_P$  and  $V_{DC}$  to odd oscillators. The amplitude of the first oscillator is monitored to ensure the initial excited strength is the same in both parts. The parameters of electric circuits and typical coupling voltages are listed in Supplementary Information.

For dynamical measurements, the real-time response of every oscillator are demodulated by fixed its frequency without coupling. All amplitudes measured in two dynamical quenching paths are showed in Fig. S4, it's normalized at every moment and showed in Fig. S4 b and d in the main text.

A sine wave sequence generated by AWG (Keysight 33522B) is an excited source before dynamical quenching. At the same time, the sequence is the reference signal for lock-in amplifier after quenching when measuring the edge oscillator. In this way, the phase demodulated by lock-in keeps the same at every measurement and the accuracy of PGP is ensured.

**Parametric Couplings.** To generate the electrostatic forces for parametric couplings between beams, an AC voltage  $V_{AC}^j(t)$  and a DC voltage  $V_{DC}$  are applied

between  $j$ -th and  $(j + 1)$ -th beam, the coupling as the following form can be generated [24].

$$L_j(t) = \frac{\partial^2 C(\delta x_j)}{\partial^2 \delta x_j} V_{AC}^j(t) V_{DC} \quad (8)$$

Here,  $C_j(\delta x_j)$  is the effective capacity between the oscillators and  $\delta x_j = x_j - x_{j+1}$ . The form of AC voltage is  $V_{AC}^j \cos(\omega_{AC}^j t)$  with  $\omega_{AC}^j = |\omega_j - \omega_{j+1}|$  and  $V_{AC}^j \ll V_{DC}$  in experiment.

The DC voltage and AC voltage are combined by a bias-tee, as showed in Fig. S2 and Fig. S3 where  $V_P$  is a sum of the neighborhood AC coupling voltage. The typical value of AC voltage used are listed in Supplementary Table S2 and Table S3.

The effective coupling strength is confirmed by measuring frequency spectrum of the response. As the Fig. S1 a shows, we measure the response of one oscillator coupled with another adjacent one. The split of peak directly describes coupling strength.

The frequency response of entire coupled chain is measured at edge oscillators, which is showed Fig. S1 c and d, correspond to topological phase and trivial phase of SSH model. Although eight peaks are not distinguishable in these spectrums because of oscillators' dissipation, the appearance of zero mode is remarkable distinction between topological and trivial. We also measure the response under equilibrium topological-trivial phase boundary, which means all coupling strengths are the same, as showed in Fig. S5.

- 
- [1] M. V. Berry, Proc. R. Soc. Lond. A **392**, 45 (1984).  
[2] D. Xiao, M.-C. Chang, and Q. Niu, *Rev. Mod. Phys.* **82**, 1959 (2010).  
[3] S. Pancharatnam, *Proceedings of the Indian Academy of Sciences - Section A* **44**, 247 (1956).  
[4] J. Samuel and R. Bhandari, *Phys. Rev. Lett.* **60**, 2339 (1988).  
[5] M. Heyl, A. Polkovnikov, and S. Kehrein, *Phys. Rev. Lett.* **110**, 135704 (2013).  
[6] J. C. Budich and M. Heyl, *Phys. Rev. B* **93**, 085416 (2016).  
[7] N. Sedlmayr, P. Jaeger, M. Maiti, and J. Sirker, *Phys. Rev. B* **97**, 064304 (2018).  
[8] C. Nayak, S. H. Simon, A. Stern, M. Freedman, and S. Das Sarma, *Rev. Mod. Phys.* **80**, 1083 (2008).  
[9] M. Z. Hasan and C. L. Kane, *Rev. Mod. Phys.* **82**, 3045 (2010).  
[10] X.-L. Qi and S.-C. Zhang, *Rev. Mod. Phys.* **83**, 1057 (2011).  
[11] F. D. M. Haldane, *Rev. Mod. Phys.* **89**, 040502 (2017).  
[12] X.-G. Wen, *Rev. Mod. Phys.* **89**, 041004 (2017).  
[13] N. Fläschner, D. Vogel, M. Tarnowski, B. Rem, D.-S. Lühmann, M. Heyl, J. Budich, L. Mathey, K. Sengstock, and C. Weitenberg, *Nature Physics* **14**, 265 (2018).  
[14] W. Sun, C.-R. Yi, B.-Z. Wang, W.-W. Zhang, B. C. Sanders, X.-T. Xu, Z.-Y. Wang, J. Schmiedmayer, Y. Deng, X.-J. Liu, S. Chen, and J.-W. Pan, *ArXiv e-prints* (2018).  
[15] M. Heyl and J. C. Budich, *Phys. Rev. B* **96**, 180304 (2017).  
[16] U. Bhattacharya, S. Bandyopadhyay, and A. Dutta, *Phys. Rev. B* **96**, 180303 (2017).  
[17] X. Qiu, T.-S. Deng, G.-C. Guo, and W. Yi, *ArXiv e-prints* (2018).  
[18] M. Heyl, *Rep. Prog. Phys.* **81**, 054001 (2018).  
[19] P. Jurcevic, H. Shen, P. Hauke, C. Maier, T. Brydges, C. Hempel, B. P. Lanyon, M. Heyl, R. Blatt, and C. F. Roos, *Phys. Rev. Lett.* **119**, 080501 (2017).  
[20] R. Bhandari and J. Samuel, *Phys. Rev. Lett.* **60**, 1211 (1988).  
[21] T. H. Chyba, L. J. Wang, L. Mandel, and R. Simon, *Opt. Lett.* **13**, 562 (1988).  
[22] W. P. Su, J. R. Schrieffer, and A. J. Heeger, *Phys. Rev. Lett.* **42**, 1698 (1979).  
[23] P. Huang, L. Zhang, J. Zhou, T. Tian, P. Yin, C. Duan, and J. Du, *Phys. Rev. Lett.* **117**, 017701 (2016).  
[24] P. Huang, P. Wang, J. Zhou, Z. Wang, C. Ju, Z. Wang, Y. Shen, C. Duan, and J. Du, *Phys. Rev. Lett.* **110**, 227202 (2013).  
[25] A. Cleland and M. Roukes, *Sensors and Actuators A: Physical* **72**, 256 (1999).  
[26] J. K. Asbóth, L. Oroszlány, and A. Pályi, *Lecture Notes in Physics* **919** (2016).  
[27] L. Zhou, Q.-h. Wang, H. Wang, and J. Gong, *ArXiv e-prints* (2017), [arXiv:1711.10741](https://arxiv.org/abs/1711.10741) [cond-mat.stat-mech].
- Acknowledgements** This work was supported by the National Key R&D Program of China (Grant No. 2018YFA0306600), the CAS (Grants No. GJJSTD20170001 and No. QYZDY-SSW-SLH004), and Anhui Initiative in Quantum Information Technologies (Grant No. AHY050000), and the Natural Science Foundation of China (NNSFC) under Grants No.11574405, 11704420 and 11675163.
- Author contributions** J.D. and C.L. conceived the project; T.T., L.Z. and P.H. designed the experimental proposal; T.T. and Z.S. prepared the experimental setup; T.T., L.Z., P.H. and S.L. performed the experiments; S.L. fabricated the sample; Y.K. and T.T. carried out the theoretical calculation; T.T., Y.K. and L.Z. carried out the numerical simulation; all authors contributed to the writing of the manuscript.
- Author information** Correspondence and requests for materials should be addressed to C.L. (lichao2@mail.sysu.edu.cn) and J.D. (djf@ustc.edu.cn).
- Competing interests** The authors declare no competing interests.

**Supplementary Information to**  
**”Direct observation of Pancharatnam geometric phase in a quenched**  
**topological system”**

(Dated: June 13, 2022)

## SSH MODEL REPRESENTED BY MECHANICAL SYSTEM

The motion of  $2N$  classical oscillators under nearest-neighboring parametric coupling can be described as:

$$m_j \ddot{x}_j + k_j x_j = -L_j(t)(x_{j+1} - x_j) - L_{j-1}(t)(x_{j-1} - x_j). \quad (\text{S1})$$

Here  $m_j$  and  $k_j = m_j \omega_j^2$  are the corresponding effective mass and spring constant,

$$L_j(t) = 2\eta_j \cos(\omega_j^p t), \quad (\text{S2})$$

is the time-dependent coupling and  $\eta_j$  is the coupling strength. For the problem concerned in this work,  $\omega_j^p$  fulfils the frequency conversion conditions:

$$\omega_j^p = (\omega_j - \omega_{j+1}) \ll \omega_j. \quad (\text{S3})$$

Using a slowly varying complex amplitudes  $\psi_j$  as  $x_j = A_j \Re(\psi_j e^{i\omega_j t})$  and ignore the terms  $\ddot{\psi}_j$ , we can get

$$i\dot{\psi}_j - \frac{L_j(t) + L_{j-1}(t)}{2m_j \omega_j} \psi_j = -\frac{L_{j-1}(t)}{2m_j \omega_j} \frac{A_{j-1}}{A_j} e^{i\omega_{j-1}^p t} \psi_{j-1} - \frac{L_j(t)}{2m_j \omega_j} \frac{A_{j+1}}{A_j} e^{-i\omega_j^p t} \psi_{j+1}, \quad (\text{S4})$$

where  $A_j = \sqrt{\hbar \omega_j / (2k_j)}$  is a constant.

According to (S2), the (S4) can be simplified by adopting the rotating wave approximation,

$$i\dot{\psi}_j = -\frac{A_{j-1}}{A_j} \frac{\eta_{j-1}}{2m_j \omega_j} \psi_{j-1} - \frac{A_{j+1}}{A_j} \frac{\eta_j}{2m_j \omega_j} \psi_{j+1}. \quad (\text{S5})$$

We introduce  $|\psi\rangle = \frac{1}{L}(\psi_1, \psi_2, \psi_3, \dots, \psi_{2N})^T$  as a single-particle wavefunction in a 1D potential. The  $L$  is a normalizing constant,  $L = \sum_j |\psi_j|^2$ . Thus, the equation of a mechanical wave (S5) is fully mapped to the Schrödinger equation,  $i\frac{d}{dt}|\psi\rangle = \hat{H}|\psi\rangle$ . By using  $|j\rangle$  to denote  $\psi_j/L$ , the Hamiltonian  $\hat{H}$  is rewritten as,

$$\hat{H} = -\sum_j \frac{\eta_j}{2} \sqrt{\frac{\omega_j \omega_{j+1}}{k_j k_{j+1}}} (|j\rangle\langle j+1| + |j+1\rangle\langle j|). \quad (\text{S6})$$

So if we set  $\eta_j \sqrt{\omega_j \omega_{j+1} / k_j k_{j+1}} / 2 = J_A (J_B)$  when  $j \in \text{odd}(\text{even})$ , this Hamiltonian represents a SSH model [1] with  $N$  unit cells.

$$\hat{H}_{\text{SSH}} = -J_A \sum_{j=2m-1} (|j\rangle\langle j| + h.c.) - J_B \sum_{j=2m} (|j\rangle\langle j| + h.c.), \quad m = 1, 2, \dots, N. \quad (\text{S7})$$

In the rest of this manuscript, we refer to the Hamiltonian of the SSH model (S7) by default when we talk about a Hamiltonian in this system.



## THE CHIRAL SYMMETRY IN THE SSH MODEL

We define a Hamiltonian  $\hat{H}$  has chiral symmetry[2], if

$$\hat{\Gamma}\hat{H}\hat{\Gamma}^\dagger = -\hat{H}, \quad (\text{S8})$$

with an operator  $\hat{\Gamma}$  fulfills these requirements:

1. The operator is unitary and hermitian,  $\hat{\Gamma}^\dagger\hat{\Gamma} = \hat{\Gamma}^2 = 1$ .
2. The operator  $\hat{\Gamma}$  is local, which means it can be represented as a direct sum of  $N$  unitary operator  $\hat{\gamma}$  acting on the internal space of each unit cell,  $\hat{\Gamma} = \hat{\gamma} \oplus \hat{\gamma} \oplus \cdots \oplus \hat{\gamma} = \bigoplus_{m=1}^N \hat{\gamma}$ .
3. The operator should be robust against some perturbations caused by some reasons including the disorder of the lattice, or the varying driven field, and so on.  $\hat{\Gamma}\hat{H}(\xi)\hat{\Gamma} = -\hat{H}(\xi)$ .

The Hamiltonian of the SSH model (S7), is usually written as follows:

$$\hat{H} = -J_A \sum_{m=1}^N (|m, B\rangle\langle m, A| + h.c.) - J_B \sum_{m=1}^{N-1} (|m+1, A\rangle\langle m, B| + h.c.). \quad (\text{S9})$$

Here it introduces two sublattice, which consist of the different sites on each unit cells. We define two orthogonal sublattice projectors  $\hat{P}_A$  and  $\hat{P}_B$ ,

$$\begin{aligned} \hat{P}_A &= \sum_{m=1}^N |m, A\rangle\langle m, A|, \quad \hat{P}_B = \sum_{m=1}^N |m, B\rangle\langle m, B|, \\ \hat{P}_A + \hat{P}_B &= 1, \quad \hat{P}_A\hat{P}_B = 0. \end{aligned} \quad (\text{S10})$$

So the chiral symmetry operator in SSH model is represented by

$$\hat{\Sigma}_z = \hat{P}_A - \hat{P}_B = \bigoplus_{m=1}^N \hat{\sigma}_z, \quad \hat{\Sigma}_z\hat{H}\hat{\Sigma}_z = -\hat{H}. \quad (\text{S11})$$

Note that this operator  $\hat{\Sigma}_z$  fulfills all the three properties mentioned above, unitary and hermitian, local and robust. For a further explanation, the relation of  $\hat{H}$  and  $\hat{\Sigma}_z$  is independent on the amplitudes of  $J_A$  and  $J_B$ , so the operator  $\hat{\Sigma}_z$  has robustness.

The chiral symmetry of Hamiltonian leads to a symmetric energy spectrum. In other words, there always exists a chiral symmetric eigenvalue  $-E_n$  ( $n = 1, 2, \dots, N$ ) for each eigenvalue  $E_n$

in SSH model ( $N$  unit cells). And the eigenstates with energy  $E_n$  and  $-E_n$  are  $|\psi_n\rangle$  and  $\hat{\Sigma}_z|\psi_n\rangle$ , respectively. This is easy to know,

$$\hat{H}|\psi_n\rangle = E_n|\psi_n\rangle, \quad \hat{H}(\hat{\Sigma}_z|\psi_n\rangle) = -\hat{\Sigma}_z\hat{H}|\psi_n\rangle = -E_n(\hat{\Sigma}_z|\psi_n\rangle). \quad (\text{S12})$$

For  $E_n \neq 0$ , the eigenstates  $|\psi_n\rangle$  and  $\hat{\Sigma}_z|\psi_n\rangle$  are orthogonal, which implies that each nonzero energy eigenstate equally supports on both sublattices[2],

$$\langle\psi_n|\hat{P}_A|\psi_n\rangle - \langle\psi_n|\hat{P}_B|\psi_n\rangle = \langle\psi_n|\hat{\Sigma}_z|\psi_n\rangle = 0. \quad (\text{S13})$$

For  $E_n = 0$ , the zero energy eigenstate supports only one sublattice. As the follow shows,  $\langle\psi_n|\hat{P}_A - \hat{P}_B|\psi_n\rangle = \pm 1$ , so either of the projections into the two sublattices vanishes alternatively.

$$\hat{H}|\psi_n\rangle = 0, \quad \hat{H}\hat{\Sigma}_z|\psi_n\rangle = 0, \quad \hat{\Sigma}_z|\psi_n\rangle = \pm|\psi_n\rangle. \quad (\text{S14})$$

Then we'll show how the dynamical phase is eliminated in a quench process from a topological edge state in the SSH model.

## ELIMINATING THE DYNAMICAL PHASE

Considering the evolution of a system of SSH model with  $N$  unit cell after a quench, the evolution follows  $|\psi(t)\rangle = e^{-i\hat{H}_f t}|\psi(0)\rangle$ . According to the definition, the dynamical quantum phase transition occurs as a nonanalytic behavior at critical times of the Loschmidt amplitude[3]:

$$\mathcal{G}(t) = r(t)e^{i\phi(t)} = \langle\psi(0)|\psi(t)\rangle = \sum_{n=1}^{2N} |\langle\psi_n|\psi(0)\rangle|^2 e^{-iE_n t}, \quad (\text{S15})$$

where  $|\psi_n\rangle$  and  $E_n$  ( $n = 1, 2, \dots, 2N$ ) are eigenstates and eigenvalues of the final Hamiltonian  $\hat{H}_f$ ,  $|\psi(0)\rangle$  is the eigenstate (or mixed state) of the initial  $\hat{H}_i$ .

In this letter, we choose a topological edge state  $|\psi(0)\rangle$  as the initial state in the quenches. According to chiral symmetry of SSH model showed above, we have  $|\langle\psi_n|\psi(0)\rangle|^2 = |\langle\psi_n|\hat{\Sigma}_z|\psi(0)\rangle|^2$  for every  $E_n \neq 0$ . Therefore, when  $\hat{H}_f$  is trivial, which means there is no zero-energy state, the Loschmidt amplitude can be rewritten as

$$\mathcal{G}(t) = 2 \sum_{m=1}^N |\langle\psi_m|\psi(0)\rangle|^2 \cos(E_m t). \quad (\text{S16})$$

Here we merge the terms of  $|\psi_m\rangle$  with energy  $E_m$  and its chiral symmetry partner  $\hat{\Sigma}_z|\psi_m\rangle$  with energy  $-E_m$ . When  $\hat{H}_f$  is non-trivial, the Loschmidt amplitude can be rewritten as

$$\mathcal{G}(t) = |\langle\psi_1|\psi(0)\rangle|^2 + |\langle\psi_1|\hat{\Sigma}_z|\psi(0)\rangle|^2 + 2 \sum_{m=2}^N |\langle\psi_m|\psi(0)\rangle|^2 \cos(E_m t), \quad (\text{S17})$$

where  $|\psi_1\rangle$  and  $\hat{\Sigma}_z|\psi_1\rangle$  denote the zero-energy eigenstates of  $\hat{H}_f$ . Either the first or the second term is zero because a topological edge state only support one sublattice.

According to (S16) and (S17), the Loschmidt amplitude is purely real in both quench processes. And in the complex plane, this amplitude can be regarded as summation of projections of  $2N$  circling motions on the real axis. These projections are pairly conjugated. So the phase  $\phi(t)$  in (S15) is either 0 or  $\pi$ , and always changes  $\pi$  when the Loschmidt amplitude  $G(t)$  passes the origin, which is defined as an occurring of the dynamical phase transition.

Without loss of generality, the phase  $\phi(t)$  consists of two parts, the geometric phase  $\phi^G(t)$  and the dynamical phase  $\phi^{\text{dyn}}(t)$ ,  $\phi^G(t) = \phi(t) - \phi^{\text{dyn}}(t)$ . We use the original name Pancharatnam geometric phase for this  $\phi^G(t)$  in order to avoid misleading to the well-known Berry phase. Here, we prove the dynamical phase  $\phi^{\text{dyn}}(t)$  is eliminated in both quenches from a topological edge state. The dynamical phase in these processes is

$$\phi^{\text{dyn}}(t) = - \int_0^t \langle\psi(s)|\hat{H}_f|\psi(s)\rangle ds = - \sum_{n=1}^{2N} |\langle\psi_n|\psi(0)\rangle|^2 E_n t. \quad (\text{S18})$$

Because of chiral symmetry,

$$- \sum_n^{2N} |\langle\psi_n|\psi(0)\rangle|^2 E_n t = \sum_{m=1}^N \left( |\langle\psi_m|\hat{\Sigma}_z|\psi(0)\rangle|^2 - |\langle\psi_m|\psi(0)\rangle|^2 \right) E_m t = 0. \quad (\text{S19})$$

The term in the summation is always 0 whether  $E_m$  is zero or not. So that the dynamical phase always keeps zero in these quenches from a topological edge state. The phase  $\phi(t)$  which we measure only has the geometric part  $\phi^G(t)$ .

## CRITICAL TIME

We choose a topological edge state of a large dimeric ( $J_A \ll J_B$ ) SSH model as the initial state in the quenches. The great advantage is that we can directly measure the PGP from the edge site. The trivial phase  $\hat{H}_{f1}$  ( $J_A^1 > J_B^1$ ) and topological phase  $\hat{H}_{f2}$  ( $J_A^2 < J_B^2$ ) are realized by coupling strength of 20Hz and 60Hz alternately in our system.

According to equation (S16), we can easily get the theoretical critical times in the quench (from  $\hat{H}_i$  to  $\hat{H}_{f1}$ ). As showed in Fig. 3 **b,c**, the two critical times are  $t_1^* = 8.45ms$  and  $t_2^* = 25.40ms$ , respectively.

## References

- [1] Su, W. P., Schrieffer, J. R. & Heeger, A. J. Solitons in polyacetylene. *Phys. Rev. Lett.*, **42**, 1698 (1979).
- [2] Asbóth, J. K., Oroszlány, L. & Pályi, A. *A Short Course on Topological Insulators*. **919**, (Springer International Publishing, 2016).
- [3] Heyl, M. Dynamical quantum phase transitions: a review. *Rep. Prog. Phys.* **81**, 054001 (2018).



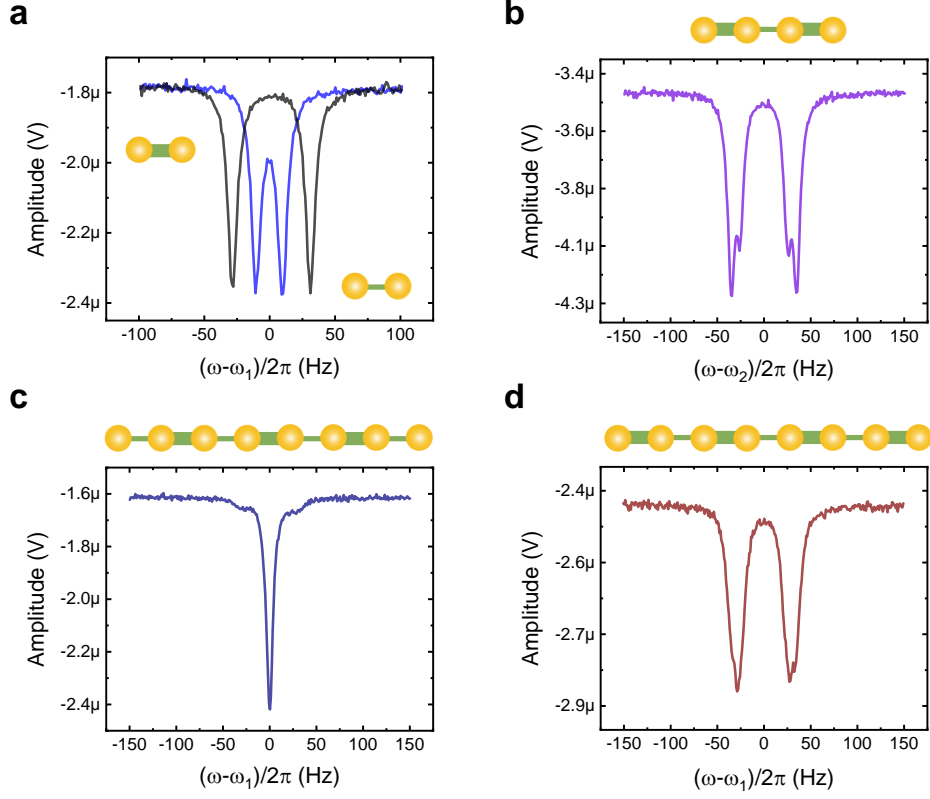


**Figure S1. Parametric couplings.** **a.** The spectrum of two coupling adjacent oscillators, which is measured at the first oscillator. The split of peaks is 20Hz or 60Hz, equaling to the coupling strength. **b.** The spectrum of four oscillators is measured at the second oscillator. The coupling strength is 60Hz and 20Hz alternately. **c.** The spectrum of the entire chain measured at the first oscillator, with coupling strength being 20Hz and 60Hz alternately. **d.** The spectrum of the entire chain measured at the first oscillator, with coupling strength being 60Hz and 20Hz alternately.

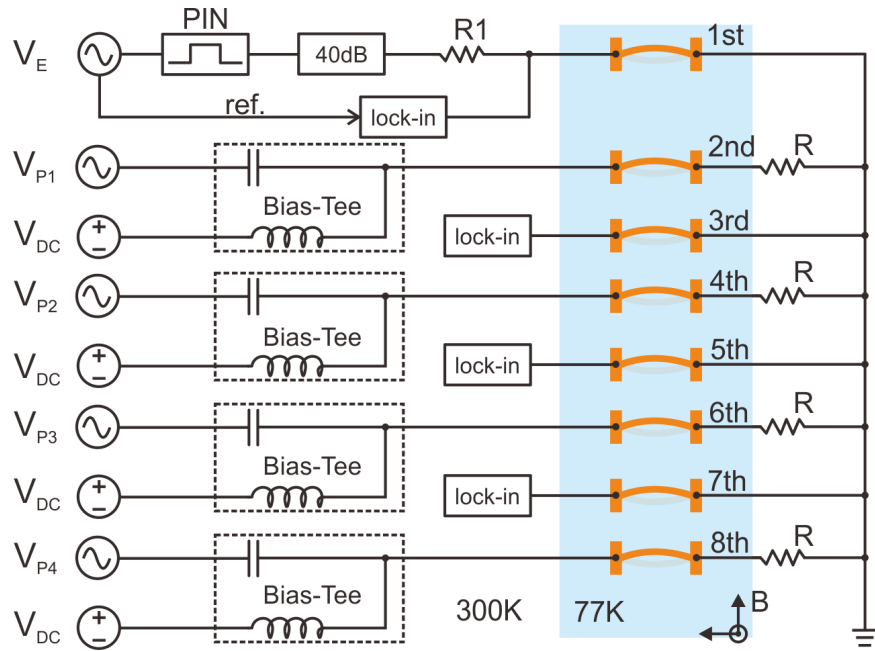


**Figure S2. Measurement circuit of odd resonators.**

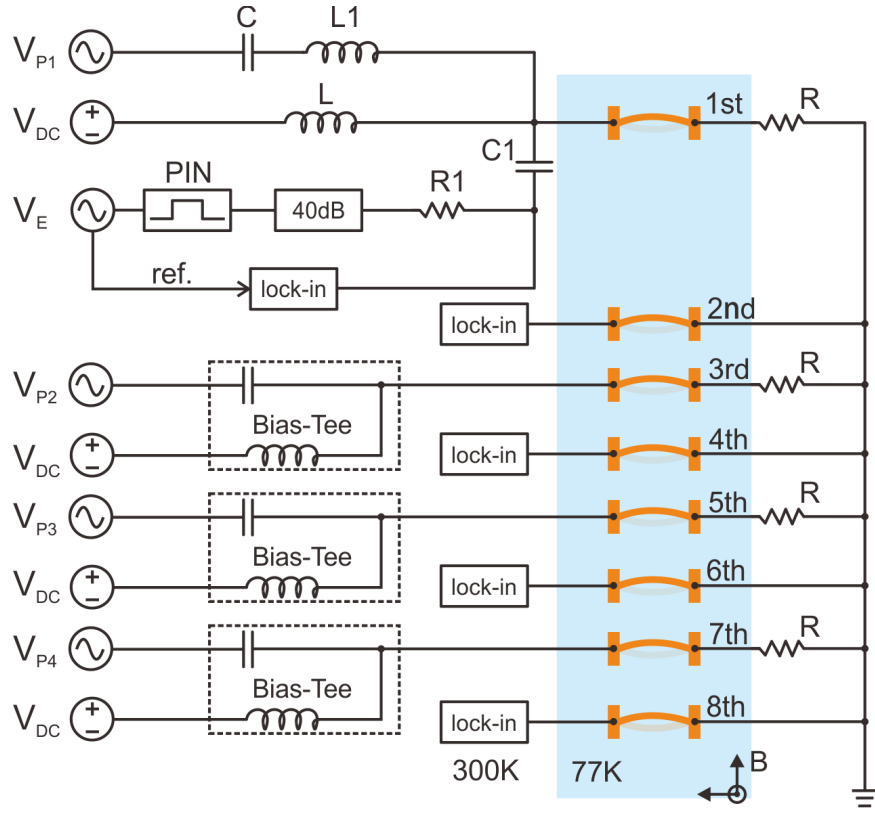


**Figure S3. Measurement circuit of even resonators.**

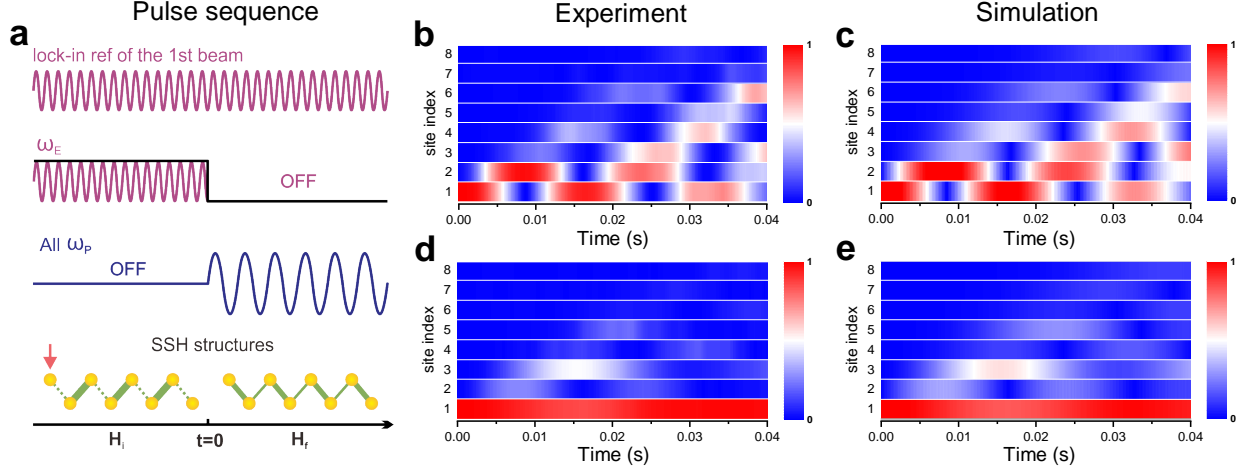


**Figure S4. Real-time dynamics after a topological edge state quenching.** **a.** The pulse sequence used in experiments. The sinusoidal wave sequence with the frequency  $\omega_E$  is used to excite the edge resonator (initial state preparation) in pre-quench and demodulate the edge resonator by lock in amplifier in post-quench. Different SSH structures in time evolution is realized by different coupling voltages. **b** and **c.** Experiment and simulation of the quench from  $\hat{H}_i$  to trivial Hamiltonian  $\hat{H}_{f1}$  (red arrow in Fig 3a). **d** and **e.** Experiment and simulation of the quench from  $\hat{H}_i$  to a topological Hamiltonian  $\hat{H}_{f2}$  (blue arrow in Fig 3a). All amplitudes showed in **b-e** are normalized at every moment.

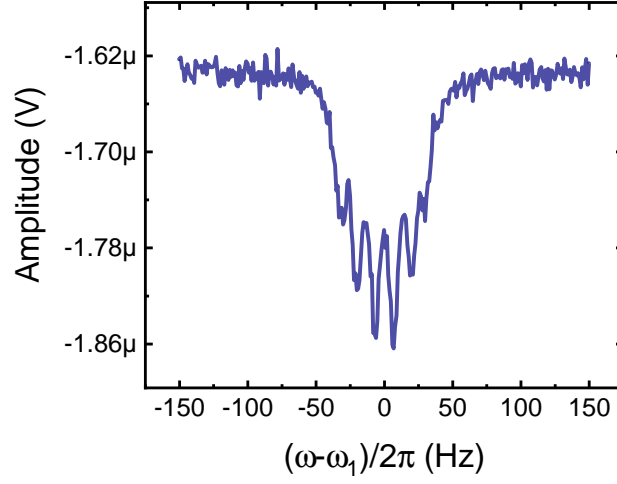


**Figure S5. The spectrum of the entire chain under the same coupling.** It's measured at the first oscillator, with all coupling strength being 40Hz. It is correspond with equilibrium topological-trivial phase boundary of SSH model.



**Table S1: The first vibrational model of oscillators**

| NO. | Frequency/kHz | Quality factor |
|-----|---------------|----------------|
| 1   | 907.184       | 106252         |
| 2   | 905.980       | 91679          |
| 3   | 923.843       | 100966         |
| 4   | 893.665       | 77447          |
| 5   | 922.695       | 105114         |
| 6   | 905.627       | 71427          |
| 7   | 918.246       | 119672         |
| 8   | 873.976       | 84012          |

**Table S2: Typical voltage used to realized coupling in Figure S2**

| $i$ | $V_{AC}^i$ (V) for topological | $V_{AC}^i$ (V) for trivial | $V_P$  |
|-----|--------------------------------|----------------------------|--|
| 1   | 0.082                          | 0.250                      | $V_{P1} = V_{AC}^1 \cos(\omega_{AC}^1 t) + V_{AC}^2 \cos(\omega_{AC}^2 t)$ |
| 2   | 0.222                          | 0.075                      |  |
| 3   | 0.069                          | 0.205                      | $V_{P2} = V_{AC}^3 \cos(\omega_{AC}^2 t) + V_{AC}^4 \cos(\omega_{AC}^4 t)$ |
| 4   | 0.207                          | 0.070                      |  |
| 5   | 0.072                          | 0.210                      | $V_{P3} = V_{AC}^5 \cos(\omega_{AC}^5 t) + V_{AC}^6 \cos(\omega_{AC}^6 t)$ |
| 6   | 0.208                          | 0.072                      |  |
| 7   | 0.072                          | 0.230                      | $V_{P4} = V_{AC}^7 \cos(\omega_{AC}^7 t)$                                  |

\* All DC voltage is the same  $V_{DC} = 4V$

**Table S3: Typical voltage used to realized coupling in Figure S3**

| $i$ | $V_{AC}^i$ (V) for topological | $V_{AC}^i$ (V) for trivial | $V_P$  |
|-----|--------------------------------|----------------------------|--|
| 1   | 0.160                          | 0.495                      | $V_{P1} = V_{AC}^1 \cos(\omega_{AC}^1 t)$                                  |
| 2   | 0.240                          | 0.079                      | $V_{P2} = V_{AC}^2 \cos(\omega_{AC}^2 t) + V_{AC}^3 \cos(\omega_{AC}^3 t)$ |
| 3   | 0.079                          | 0.232                      |  |
| 4   | 0.214                          | 0.073                      | $V_{P3} = V_{AC}^4 \cos(\omega_{AC}^4 t) + V_{AC}^5 \cos(\omega_{AC}^5 t)$ |
| 5   | 0.073                          | 0.222                      |  |
| 6   | 0.220                          | 0.074                      | $V_{P4} = V_{AC}^6 \cos(\omega_{AC}^6 t) + V_{AC}^7 \cos(\omega_{AC}^7 t)$ |
| 7   | 0.085                          | 0.245                      |  |

\* All DC voltage is the same  $V_{DC} = 4V$

**Table S4: Parameters of the electric circuit in Figure S2 and S3**

$$R1=4k\Omega$$

$$R=1M\Omega$$

$$C=680nF$$

$$C1=1nF$$

$$L=2.2mH$$

$$L1=10mH$$

---

\* All Bias-Tee blocks are made up of C and L